



Cite this: *RSC Adv.*, 2020, **10**, 44225

Received 20th October 2020
 Accepted 26th November 2020

DOI: 10.1039/d0ra08920f

rsc.li/rsc-advances

Photoelectrochemical enzymatic sensor for glucose based on Au@C/TiO₂ nanorod arrays†

Lianyuan Ge,^a Rui Hou,^a Yang Cao,^{ac} Jinchun Tu^a and Qiang Wu^a

In this work, a photoelectrochemical (PEC) glucose biosensor was synthesized on the basis of a type of Au@C/TiO₂ composite by using an unsophisticated secondary hydrothermal strategy. The compounded Au@C/TiO₂ material was characterized by XRD, SEM, TEM, UV-vis, and XPS to identify the composition and the purity of the phase. Glucose oxidase (GODx) was immobilized on the Au@C/TiO₂. The PEC biosensor presented satisfactory stability and outstanding reproducibility. The range and the sensitivity of the linear measurement were 0.1–1.6 mM and 29.76 $\mu\text{A mM}^{-1} \text{cm}^{-2}$, respectively, and the detection limit was low (0.049 mM). The GODx/Au@C/TiO₂/FTO biosensor presented excellent efficiency in detecting glucose, suggesting the great potential application of this synthesized material in PEC biosensors.

1. Introduction

Photoelectrochemical (PEC) biosensors have drawn great attention recently because of many advantages, such as low background, low cost, and high sensitivity.¹ PEC biosensors are dependent on photoactive semiconductor nanomaterials and exhibit excellent performance. Particularly, its photoactivity has an essential part in the determination of the function of biosensors in analysis.^{2,3}

TiO₂, a semiconductor with a wide n-type band gap, is considered as a promising material in the detection of biomolecules in the heterogeneous photocatalysis due to its high chemical stability, low cost, nontoxicity, and excellent oxidizing power.^{4–7} Compared with other semiconductor materials, TiO₂ is suitable to be applied in photocatalytic activities because of its high photoactivity and porosity.^{8,9} Nonetheless, as a kind of photocatalyst, TiO₂ is not used extensively due to large band gap energy ($E_g = 3.2$ eV), and fast recombination rate of photoelectron–hole pairs, which limits the utilization of TiO₂ in the visible light range.^{10,11} Several methods, such as dye bonding on the surface of TiO₂, metal nanoparticles and nonmetal deposition, connecting narrow-band gap semiconductors, can

be used to enhance the activity of the visible light for TiO₂ and solve the aforementioned problems.^{12–14}

Glucose (Glu) is considered as the main source for generating energy in cellular modulation and metabolism and shows an important position in the cellular growth. The lack or the excess of Glu may cause adverse effects on the function of cells. The sensitive and rapid assessment of the level of Glu, as one of the indicators for diabetes, in the urine and the blood is important.^{15–18}

Generally, carbon (C) owns inherent benefits, including high stability, low cost, and improved electrical conductivity, and better biocompatibility. Moreover, C materials can improve the adsorption of enzymes and increase the detection range and the sensitivity of the enzyme sensors. Given that metal NPs(nano-particles) can concentrate light near the semiconductor/liquid junction to generate photocarriers that can reach the interface, the proper integration of the surface plasmon resonance (SPR) enhanced photoelectrochemistry and well-designed biological reactions is possible and provides great opportunities for new biomolecule detection.¹⁹ Moreover, the nanoparticles made of noble metal can produce intermediates that can capture or transfer photo-generated electrons.²⁰

Therefore, TiO₂ nanorods, a novel enzyme Glu sensor, is constructed by integrating the advantages of C and Au. The synthesis of Au@C/TiO₂ nanorod arrays (NRAs) is shown in Scheme 1. The TiO₂ NRAs are obtained using a common hydrothermal approach. Au nanoparticles and the C shell are deposited onto the surface of TiO₂ NRAs by using the secondary hydrothermal approach. The PEC biosensor of Glu is developed using Glu oxidase (GODx) over the surface of Au@C/TiO₂ NRAs, which is coated with the electrode of F-doped SnO₂ (FTO). The acquired PEC biosensor presents satisfactory reproducibility and outstanding stability. Additionally, the detection limit is low (0.049 mM). The range of linear measurement and the

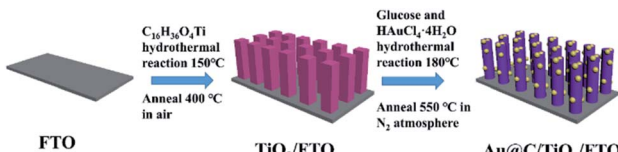
^aKey Laboratory of Advanced Materials of Tropical Island Resources, State Key Laboratory of Marine Resource Utilization in South China Sea, Hainan University, Haikou 570228, P. R. China. E-mail: tujinchun@hainu.edu.cn

^bSchool of Tropical Medicine and Laboratory Medicine, Key Laboratory of Emergency and Trauma of Ministry of Education, Hainan Medical University, Haikou 571199, China. E-mail: wuqiang001001@aliyun.com

^cKey Laboratory of Child Cognition & Behavior Development of Hainan Province, Qiongtai Normal University, Haikou 571127, P. R. China

† Electronic supplementary information (ESI) available: XRD patterns of TiO₂, C/TiO₂, Au/TiO₂ and Au@C/TiO₂ between 15° and 30°; electron lifetime measurements of TiO₂, C/TiO₂, Au/TiO₂, Au@C/TiO₂; Mott–Schottky plots of TiO₂, C/TiO₂, Au/TiO₂, Au@C/TiO₂. See DOI: [10.1039/d0ra08920f](https://doi.org/10.1039/d0ra08920f)





Scheme 1 Au@C/TiO₂/FTO fabrication.

sensitivity of the PEC biosensor are 0.1–1.6 mM and 29.76 $\mu\text{A mM}^{-1} \text{cm}^{-2}$, respectively.

2. Experimental

2.1. Reagents and materials

Outhwaite New Energy Company provided FTO glasses. Tetra-butyl titanate ($\text{C}_{16}\text{H}_{36}\text{O}_4\text{Ti}$) was available from Tianjin Fuchen Chemical Reagent Factory. Ethanol ($\text{CH}_3\text{CH}_2\text{OH}$), isopropyl alcohol ($\text{CH}_3\text{CH}_2\text{CHOH}$), and hydrochloric acid (HCl) were the products of the Xilong Science Corporation. Glucose anhydrous ($\text{C}_6\text{H}_{12}\text{O}_6$) was provided by Guangzhou Chemical Reagent Factory. Glucose oxidase (GODx) was gained from Shanghai Bioengineering Co. Ltd. HAuCl₄·4H₂O was from Sinopharm Chemical Reagent Co., Ltd. Materials were not further purification. Liquid solutions prepared by ultrapure water.

2.2. Synthesis of TiO₂ NRAs

TiO₂ NRAs were grew on the FTO glass substrate by using a previously reported hydrothermal method.²¹ First, FTO glass substrates were ultrasonically cleaned by sonicating in isopropyl alcohol, acetone and ultrapure water. Second, 20 ml HCl was added into 20 ml ultrapure water, and the solution was stirred for 10 min, added with 0.4 ml tetrabutyl titanate, stirred vigorously for about 30 min and added with Teflon (30 ml). The mixture was placed onto a clean FTO glass substrate at an angle lying against the Teflon wall. The Teflon was sealed and heated for 4 h at 150 °C in an oven, and the autoclave was cooled to room temperature naturally. Finally, the sample was dried, washed with ultrapure water, and annealed for 2 h at 400 °C in air.

2.3. Synthesis of C/TiO₂ NRAs

C/TiO₂ NRAs were constructed using a simple hydrothermal approach. Anhydrous Glu (0.36 g) was added with 20 ml ultrapure water, and the Glu solution was stirred for 10 min, added with Teflon, and placed onto the FTO glass substrate with TiO₂ NRAs at an angle lying against the Teflon wall. The Teflon was sealed and heated for 4 h at 180 °C in an oven, and the autoclave was cooled to room temperature naturally. Finally, the sample was dried, washed using ultrapure water, and annealed for 2 h at 550 °C in an N₂ atmosphere.

2.4. Synthesis of Au/TiO₂ NRAs

Au/TiO₂ NRAs were synthesized using a simple hydrothermal approach. HAuCl₄·4H₂O (0.02 ml, 1%) was added with 20 ml ultrapure water, and the mixture was stirred for 10 min, added

with the Teflon, and placed onto the FTO glass substrate with TiO₂ NRAs at an angle lying against the Teflon wall. The Teflon was sealed and heated for 4 h at 180 °C in an oven, and the autoclave was cooled to room temperature naturally. Finally, the sample was dried, washed using ultrapure water, and annealed for 2 h at 550 °C in an N₂ atmosphere.

2.5. Synthesis of Au@C/TiO₂ NRAs

Au@C/TiO₂ NRAs were synthesized using a hydrothermal approach. Anhydrous Glu (0.36 g) was added with 20 ml ultrapure water, and the solution was stirred for 10 min, added with 1% HAuCl₄·4H₂O (0.02 ml), stirred for 10 min, added with the Teflon, placed onto the FTO glass substrate with TiO₂ NRAs at an angle lying against the Teflon wall. The Teflon was sealed and heated for 4 h at 180 °C in an oven, and the autoclave was cooled to room temperature naturally. Finally, the sample was dried, washed using ultrapure water, and annealed for 2 h at 550 °C in an N₂ atmosphere.

2.6. Constructing of the PEC electrode

The Au@C/TiO₂ NRAs FTO electrode and the GODx solution (10 mg ml⁻¹) were prepared to establish the biosensor of GODx/Au@C/TiO₂ NRAs. The GODx solution 20 μL was used on the Au@C/TiO₂ NRAs FTO electrode, which was dried at 4 °C for 48 h.

2.7. Detection and instruments

The morphology characteristics of the surface of the PEC electrode were assessed with the field emission scanning electron microscope (FESEM, Hitachi S-3000 4800). The images of TEM were obtained by using the transmission electron microscopy (Tecnai G2 20). The crystal structures were measured by using the analysis of X-ray diffraction (XRD) instrument of D8 Tools XRD. The voltage was set as 40 kV, and the current as 30 mA with Cu-K α radiation ($k = 1.5406 \text{ \AA}$). The UV-vis absorption spectrophotometer (JASCO, UV-550) was used to obtain the UV-vis absorption spectrum, and the wavelength was set as 300–800 nm. We used the multifunctional imaging electron spectrometer (Thermo ESCALAB 250XI) to perform X-ray photoelectron spectroscopy (XPS). The CHI 660C workstation (CHI Instruments, Chenzhua, Shanghai, China) combined with a 500 W Xenon lamp was applied to perform the PEC tests. Traditional electrochemical system with three electrodes was utilized in the PBS buffer (pH = 7.4) solution in room temperature, and the GODx/Au@C/TiO₂ electrode was used as the working electrode. Meanwhile, Pt foil functioned as the counter electrode and Ag/AgCl as the reference electrode.

3. Results and discussion

Fig. 1 shows the XRD patterns of the samples. The peaks of FTO substrates were indexed in accordance with the database of JCPDS (46-1688), whereas the peaks of samples were indexed in accordance with the database of JCPDS (21-1276). The samples were discovered to own rutile TiO₂ tetragonal structures. The peaks at 27.45°, 36.08°, 54.32°, 62.74°, 69.01°, and 69.79° were



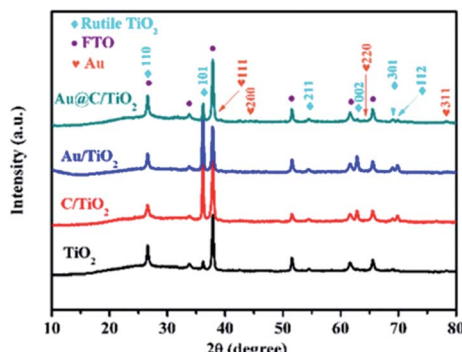


Fig. 1 XRD patterns of TiO_2 , C/TiO_2 , Au/TiO_2 , and $\text{Au}@\text{C}/\text{TiO}_2$.

associated with the planes of (110), (101), (211), (002), (301), and (112), respectively. The Au/TiO_2 and the $\text{Au}@\text{C}/\text{TiO}_2$ samples were indexed in accordance with the database of JCPDS (04-0784), and Au nanoparticles were found. The C/TiO_2 and the $\text{Au}@\text{C}/\text{TiO}_2$ samples had a slightly increased peak between 20° and 25° (Fig. S1†) and showed that the C shell had successfully grown on the TiO_2 .²²

Fig. 2 shows the SEM images of TiO_2 , C/TiO_2 , Au/TiO_2 and $\text{Au}@\text{C}/\text{TiO}_2$. As shown in Fig. 2A–C, rutile TiO_2 NRAs were successfully attached to the FTO substrates. The diameter and the length of TiO_2 NRAs were approximately 60–120 nm and about 1–2 μm , respectively. As shown in Fig. 2D–F, with the addition of C, no evident change was observed in C/TiO_2 compared with TiO_2 . Only parts of the TiO_2 NRAs were covered with a thin layer of C. As shown in Fig. 2G–I, some Au nanoparticles with size of 5–40 nm were attached onto TiO_2 NRAs. As shown in Fig. 2J–L, with the addition of C and Au nanoparticles at the same time, $\text{Au}@\text{C}$ composites covered TiO_2 NRAs. The thickness of the $\text{Au}@\text{C}$ composites was approximately 200–

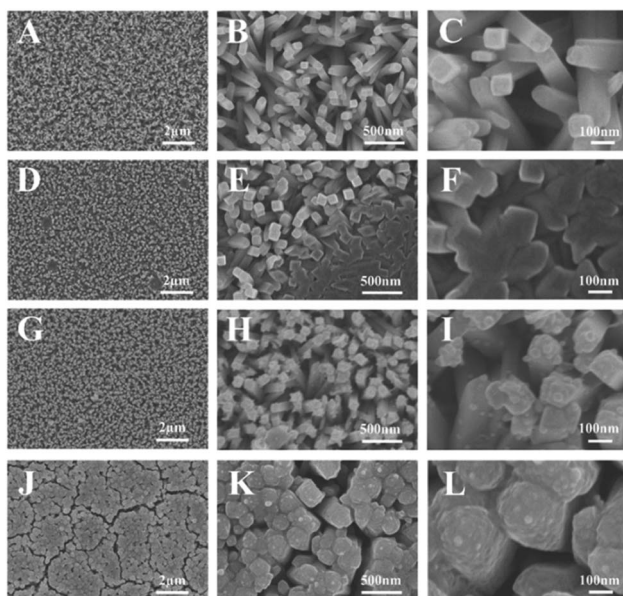


Fig. 2 SEM images of (A–C) TiO_2 , (D–F) C/TiO_2 , (G–I) Au/TiO_2 , (J–L) $\text{Au}@\text{C}/\text{TiO}_2$.

300 nm and Au nanoparticles had a size of about 5–40 nm. The $\text{Au}@\text{C}$ composites structure may facilitate the transport of photogenerated electrons, thereby inhibiting the recombination of photogenerated electrons and holes.

The HRTEM and the TEM images of $\text{Au}@\text{C}/\text{TiO}_2$ and TiO_2 are shown in Fig. 3A–F, respectively. The $\text{Au}@\text{C}/\text{TiO}_2$ and the TiO_2 samples demonstrated similar morphological features in TiO_2 nanorods. The diameter of TiO_2 nanorods was approximately 120 nm. Given that the C and the Au gradually attached to the TiO_2 nanorods, these nanorods were covered with the $\text{Au}@\text{C}$ composites. Au nanoparticles had a size of about 5–40 nm. The lattice margins of $\text{Au}@\text{C}/\text{TiO}_2$ and TiO_2 (Fig. 1B and E) were 0.324 nm, which corresponded to the (110) crystal plane of the rutile TiO_2 . The lattice fringe of $\text{Au}@\text{C}/\text{TiO}_2$ (Fig. 1F) was 0.235 nm, which corresponded to the (111) crystal plane of Au nanoparticles. The composition of $\text{Au}@\text{C}/\text{TiO}_2$ was revealed using elemental mapping and HAADF-STEM imaging (Fig. 1G). Ti, O, C, and Au elements were uniformly distributed in $\text{Au}@\text{C}/\text{TiO}_2$. Moreover, the C encased the Au particles, which were scattered on the surface of the TiO_2 nanorods. The co-existence of Au and C would facilitate the transmission of electrons. At the same time, the $\text{Au}@\text{C}$ composites structure would facilitate the adsorption of GODx.

The UV-vis spectra of $\text{Au}@\text{C}/\text{TiO}_2$, Au/TiO_2 , C/TiO_2 and TiO_2 are shown in Fig. 4A. Their bandgap values were obtained using the Kubelka–Munk function (Fig. 4B).²³ The absorption band and the bandgap value of the TiO_2 was at about 405 nm (Fig. 4A) and 3.06 eV (Fig. 4B), respectively. TiO_2 was a typical rutile. C/TiO_2 showed an escalated absorption peak (416 nm, Fig. 4A) and lower bandgap value (2.98 eV, Fig. 4B) in comparison with TiO_2 , suggesting that the C was successfully deposited onto the TiO_2 surface, and a small amount of C was doped into the TiO_2 . The absorption band and the bandgap value of Au/TiO_2 were about 406 nm (Fig. 4A) and 3.06 eV (Fig. 4B), respectively. The Au/TiO_2 was observed with an evident absorption band from 500 nm to 600 nm (Fig. 4A), which was attributed to the SPR absorption of the Au nanoparticles. This

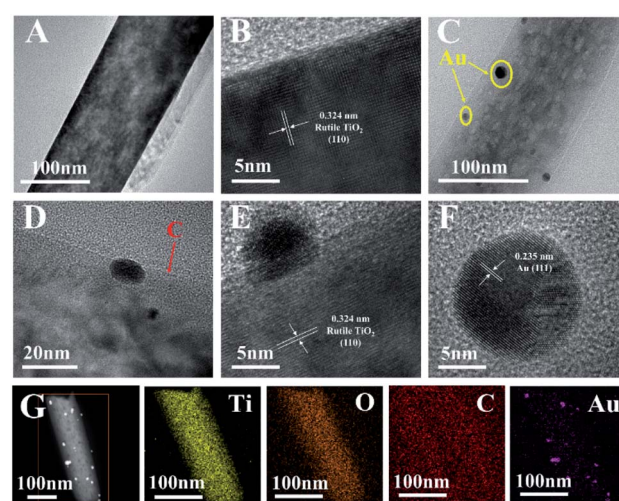


Fig. 3 (A) TEM, (B) HRTEM of TiO_2 . (C and D) TEM, (E and F) HRTEM, (G) HAADF-STEM and element mappings of Ti, O, C, Au of $\text{Au}@\text{C}/\text{TiO}_2$.

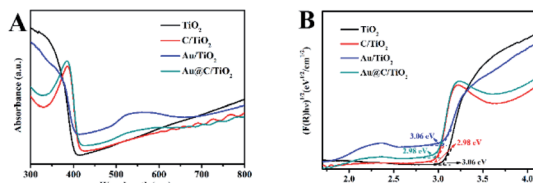


Fig. 4 (A) UV-vis absorption spectra, (B) plots of $(F(R)hv)^{1/2}$ vs. E (eV) for TiO_2 , C/TiO_2 , Au/TiO_2 and $\text{Au}@\text{C}/\text{TiO}_2$.

result implied the deposition of Au nanoparticles on the TiO_2 surface. The $\text{Au}@\text{C}/\text{TiO}_2$ had higher absorption peak (416 nm, Fig. 4A) and lower bandgap value (2.98 eV, Fig. 4B) compared with the TiO_2 . These results implied that the C and the Au were deposited onto the TiO_2 surface and that the $\text{Au}@\text{C}$ was formed on the TiO_2 surface. A small amount of C may be doped into TiO_2 . A new peak at 500–600 nm was observed in $\text{Au}@\text{C}/\text{TiO}_2$ (Fig. 4A) and attributed to the SPR absorption of Au nanoparticles.

As shown in Fig. 5A, the XPS survey spectra suggested that the $\text{Au}@\text{C}/\text{TiO}_2$ consisted of Au, C, Ti and O. Fig. 5B displays the O 1s spectra. Three intense peaks at 531.6, 530.3, and 529.1 eV, corresponding to the $\text{C}=\text{O}$ bonds, $\text{C}-\text{O}$, and $\text{Ti}-\text{O}$ bonds (lattice O), respectively, were observed in the samples.²⁴ The C 1s spectra are shown in Fig. 5C. The peaks at 287.8 and 284.6 eV might result from the bonds of $\text{C}-\text{O}$ and $\text{C}-\text{C}$.²⁴ Fig. 5D shows the Ti 2p spectra of the core level with a high resolution. The

XPS peaks of $\text{Ti} 2p_{1/2}$ and $2p_{3/2}$, which had excellent symmetry with the TiO_2 sample, appeared at about 463.6 and 457.9 eV, suggesting that the chemical valence of Ti^{4+} appeared to have an octahedral coordination with O.²⁵ The binding energy difference (ΔE) between $\text{Ti} 2p_{3/2}$ and $\text{Ti} 2p_{1/2}$ was about 5.7 eV, indicating that the chemical state of Ti was Ti^{4+} .²⁴ In Fig. 5E, the XPS spectra of $\text{Au}@\text{C}/\text{TiO}_2$ presented the peaks of $\text{Au} 4f_{5/2}$ and $\text{Au} 4f_{7/2}$ centered at 86.5 and 82.8 eV, respectively. The spin energy separation of 3.7 eV was highly consistent with the published results about $\text{Au} 4f_{5/2}$ and $\text{Au} 4f_{7/2}$ in Au nanoparticles.²⁶

In Fig. 6, the electrochemical and the PEC experiments were performed to detect the PEC performance of TiO_2 , Au/TiO_2 , $\text{Au}@\text{C}/\text{TiO}_2$, and C/TiO_2 samples under illumination. In Fig. 6A, linear sweep voltammograms (LSV) highlighted the conclusions as follows. (1) C/TiO_2 , Au/TiO_2 , and $\text{Au}@\text{C}/\text{TiO}_2$ samples showed enhanced photocurrent densities than TiO_2 , indicating that the inter-bands in C-Au, C, and Au-depositions and the SPR from Au nanoparticles created a light response for the TiO_2 -based photoelectrode. (2) The $\text{Au}@\text{C}/\text{TiO}_2$ demonstrated the highest photocurrent density among all samples and had significantly higher photocurrent density than the C/TiO_2 from the Au/TiO_2 samples.

The inherent electronic features were detected using electrochemical impedance spectra (EIS) and open-circuit photovoltage decay (OCPVD) experiments to further understand the performance of PEC. OCPVD experiments were performed, and the electron lifetime generated by photo was estimated in accordance with the following formula:²⁷

$$\tau = \frac{k_B T}{e} \left(\frac{dV_{OC}}{dt} \right)^{-1}.$$

In the equation, τ represents the photoelectron lifetime dependent on the potential, T represents temperature, k_B represents the Boltzmann's constant, V_{OC} stands for the open-circuit voltage at time t , and e represents the charge in a single electron. As shown in Fig. S2,† the $\text{Au}@\text{C}/\text{TiO}_2$ sample presented the longest lifetime of the electron, which contributed to the high performance of PEC. The EIS was considered as one of the powerful tools in the study of the interfacial features of photoelectrodes. Fig. 6B presents the Nyquist plots. The $\text{Au}@\text{C}/\text{TiO}_2$ demonstrated the smallest diameter of the semi-circle, indicating the lowest resistance in charge transfer and the fastest mobility of the electron. The measurement of capacitance of the electrolyte/electrode was performed to detect

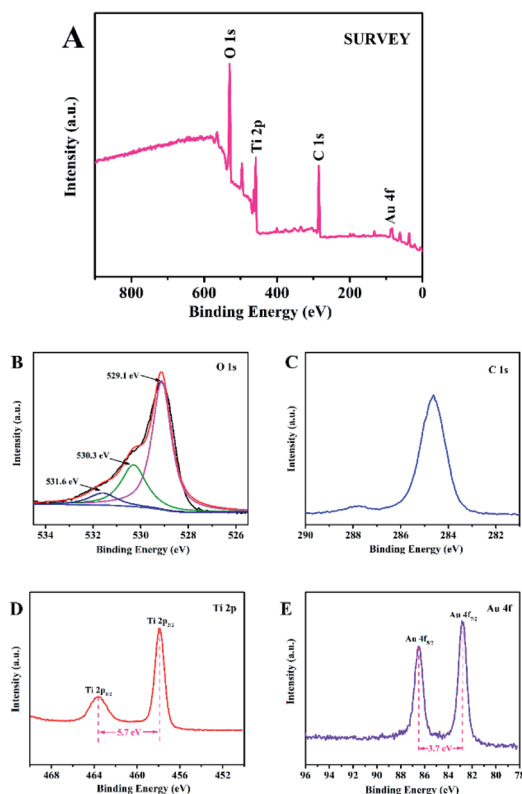


Fig. 5 XPS patterns of (A) survey spectra, (B) O 1s, (C) C 1s, (D) Ti 2p, (E) Au 4f.

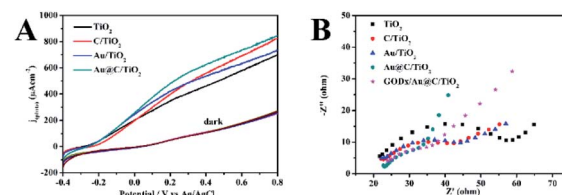


Fig. 6 Photoelectrochemical performance of TiO_2 , C/TiO_2 , Au/TiO_2 , $\text{Au}@\text{C}/\text{TiO}_2$ in (A) linear-sweep voltammograms, collected at a scan rate of 0.1 V s^{-1} under illumination, (B) electrochemical impedance spectra of Nyquist plots.



the carrier density (N_D) in accordance with the following formula:²⁸

$$\frac{1}{C^2} = \frac{2}{N_D e \epsilon_0 \epsilon} \left[(U_S - U_{FB}) - \frac{k_B T}{e} \right].$$

In this equation, C stands for the capacitance of the space charge in the semiconductor, N_D represents the density of the electron carrier, e is the elemental charge, ϵ_0 represents the vacuum permittivity, ϵ is defined as the relative permittivity of the semiconductor, U_S is the applied potential, T represents temperature, and k_B stands for the Boltzmann constant. The N_D was measured as $1/C^2$ vs. potential (Fig. S3†) by using the Mott-Schottky (MS) plots through the equation as follows:²⁸

$$N_D = - \left(\frac{2}{e \epsilon \epsilon_0} \right) \left(\frac{d \left(\frac{1}{C^2} \right)}{d(U_S)} \right)^{-1}.$$

The calculated donor densities followed the order: $\text{TiO}_2 < \text{Au}/\text{TiO}_2 < \text{C}/\text{TiO}_2 < \text{Au}@\text{C}/\text{TiO}_2$. The significantly increased N_D confirmed that the C-Au-deposition could improve the electric conductivity, and accelerate the electron transfer.

Photocurrent responses used C/TiO_2 , TiO_2 , $\text{Au}@\text{C}/\text{TiO}_2$, Au/TiO_2 and $\text{GODx}/\text{Au}@\text{C}/\text{TiO}_2$ as the photoanodes under irradiation. The photocurrent-time curves of these samples are demonstrated in Fig. 7A. The photocurrents in the five samples were remarkably raised to the net saturated values and decreased to 0, which was consistent with the irradiation by light turned off and on. The results of PEC demonstrated that the $j(\text{photo})$ values followed the order: $\text{Au}@\text{C}/\text{TiO}_2 > \text{C}/\text{TiO}_2 > \text{Au}/\text{TiO}_2 > \text{GODx}/\text{Au}@\text{C}/\text{TiO}_2 > \text{TiO}_2$. The $\text{Au}@\text{C}/\text{TiO}_2$ showed the largest photocurrent ($362 \mu\text{A cm}^{-2}$), which was followed by C/TiO_2 ($309 \mu\text{A cm}^{-2}$), Au/TiO_2 ($305 \mu\text{A cm}^{-2}$), $\text{GODx}/\text{Au}@\text{C}/\text{TiO}_2$ ($274 \mu\text{A cm}^{-2}$), and TiO_2 ($268 \mu\text{A cm}^{-2}$). The photocurrent of C/TiO_2 was 1.15 times that of TiO_2 . This may be due to the fact that the TiO_2 was coated with the carbon layer, and the carbon shell was beneficial to absorb light. At the same time, the carbon itself had good conductivity, which was beneficial to the transmission of electrons. And it reduced the coincidence of photo-generated electrons and holes to improve its photoelectric performance. The photocurrent of Au/TiO_2 was 1.14 times that of TiO_2 . Due to the SPR effect of gold nanoparticles, its light absorption in the visible light region was enhanced. The conductivity of gold nanoparticles themselves was also excellent, and their electron transfer ability was enhanced, resulting in photocurrent improve. Approximately 1.35-fold increment in the produced photocurrent was acquired from TiO_2 to $\text{Au}@\text{C}/\text{TiO}_2$ due to two main reasons. First, the SPR from Au nanoparticles and the electrons transfer to the C shell and the TiO_2 . Second, the C-Au-deposition process accelerated the electron transfer and enhanced the separation efficiency for photo-generated electron-hole pairs.

As shown in Fig. 7B, the photocurrent increased as the Glu concentration increased on the $\text{GODx}/\text{Au}@\text{C}/\text{TiO}_2$ electrode, which demonstrated a sensitive reaction to the concentration of

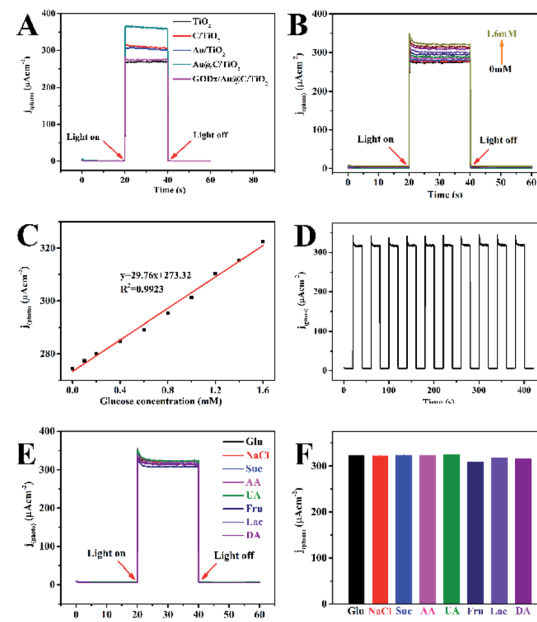


Fig. 7 (A) The $j(\text{photo})-t$ responses of TiO_2 , C/TiO_2 , Au/TiO_2 , $\text{Au}@\text{C}/\text{TiO}_2$ and $\text{GODx}/\text{Au}@\text{C}/\text{TiO}_2$ in 0.1 M pH 7.4 PBS at 0.4 V vs. Ag/AgCl , (B) the $j(\text{photo})-t$ responses of $\text{GODx}/\text{Au}@\text{C}/\text{TiO}_2$ toward Glu at increasing concentration from 0 mM to 1.6 mM in the supporting electrolyte of 0.1 M pH 7.4, (C) linear calibration ($[\text{Glu}]$ vs. $j(\text{photo})$) curve. (D) Stability of $\text{GODx}/\text{Au}@\text{C}/\text{TiO}_2$ electrode with 1.6 mM glucose, (E and F) Effect of interferences on the response photocurrents. Experiments were performed in 0.1 M pH 7.4 PBS containing 1.6 mM of Glu with NaCl, Suc, AA, UA, Fru, Lac and DA with light ON.

Glu. As shown in Fig. 7C, the linear regression equation between Glu concentrations and the photocurrent was $j (\mu\text{A cm}^{-2}) = 29.76X + 273.32$ (mM). Thus, the sensitivity was measured as $29.76 \mu\text{A mM}^{-1} \text{cm}^{-2}$ at Glu concentration of 0.1 mM to 1.6 mM. The detection limit ($3S/N$) was 0.049 mM. Where S was the slope of the calibration curve and N was the standard deviation of blank samples signals. Moreover, the $\text{GODx}/\text{Au}@\text{C}/\text{TiO}_2$ biosensor stability was featured through the responses of $j(\text{photo})-t$, whereas the light was turned OFF/ON iteratively 10 times in PBS (0.1 M, pH 7.4; Fig. 7D). If light was turned on, the $j(\text{photo})$ response increased rapidly and stayed stable in seconds. The $\text{GODx}/\text{Au}@\text{C}/\text{TiO}_2$ biosensor remained stable and fluctuated negligibly with time even after 10 cycles.

The effects of highly probable coexisting and usual molecular interfering species (such as NaCl, sucrose (Suc), ascorbic acid (AA), uric acid (UA), fructose (Fru), lactose (Lac) and dopamine (DA)), which may influence the response of the $\text{GODx}/\text{Au}@\text{C}/\text{TiO}_2$ biosensor, was investigated. PEC experiments were performed under the same conditions as the detection of PEC Glu to discover the selectivity of the biosensor of $\text{GODx}/\text{Au}@\text{C}/\text{TiO}_2$. In addition, the interfering species (0.1 mM) was added into the solution (Fig. 7E). The variance of $j(\text{photo})$ after the addition of interfering species was calculated using the plots of $j(\text{photo})-t$. In Fig. 7E and F, no significant response was found in the detection of PEC Glu following the



Table 1 Comparisons of analytical characteristics between the specific sensor and the other sensors used in detecting glucose

Biosensor composition	Linear range/(mM)	Sensitivity/ ($\mu\text{A mM}^{-1} \text{cm}^{-2}$)	Reference
GODx/SnS ₂ /Nafion/GCE	0.025–1.10	7.6	29
GCE/GODx/Nafion/Br[Demim]/TNT-AuNP	0.01–1.2	5.1	30
Nafion/GODx/Ag-Pdop@CNT/GCE	0.05–1.10	3.1	31
GODx/TCS-TiO ₂ /chitosan/GCE	0.005–1.32	23.2	32
GODx/CNx-MWCNT/GCE	0.02–1.02	13	33
GODx/Au@C/TiO ₂ /FTO	0.1–1.6	29.76	This work

addition of the molecular interfering species. This response may result from the facilitation by the surface GODx fixed on the Au@C/TiO₂. Results proved that the constructed PEC biosensor in accordance with the GODx/Au@C/TiO₂ showed outstanding and specific selectivity to the Glu biosensor.

The analytical performance of the GODx/Au@C/TiO₂/FTO biosensors was compared with those of other Glu sensors (Table 1) and showed good results in terms of sensitivity and linear range.

The plausible mechanisms for the PEC Glu detection on the GODx/Au@C/TiO₂/FTO biosensor under light ON were determined.

As shown in Scheme 2, the C and the Au deposited on the surface of TiO₂ was essential in the migration process of generated electrons and holes of the PEC and could minimize their recombination. Under light illumination, the SPR effect of Au nanoparticles and electrons were transferred to the C shell. The electrons in the TiO₂ valence band were excited to the conduction band. Electrons were transferred to the conduction band of TiO₂ from the C shell. Finally, electrons were transferred to the FTO substrate. The process accelerated the electron transfer rate and inhibited the recombination rate of the hole–electron pairs. The process prolonged the electron lifetime and increased the concentration of carriers. The group of the flavin adenine dinucleotide (FAD) redox in the GODx could oxidize Glu analytes into gluconic acids, which turned into the reduced flavine adenine dinucleotide (FADH₂) with enhanced shifting and close attachment to the PEC. The GODx on the Au@C/TiO₂ surface could reduce O₂ into H₂O₂. At the same

time, the photogenerated holes from the valence band of TiO₂ could move. Electrons could migrate onto the Au@C/TiO₂ surface, which was consumed by H₂O₂ to form a flow of charge.

4. Conclusions

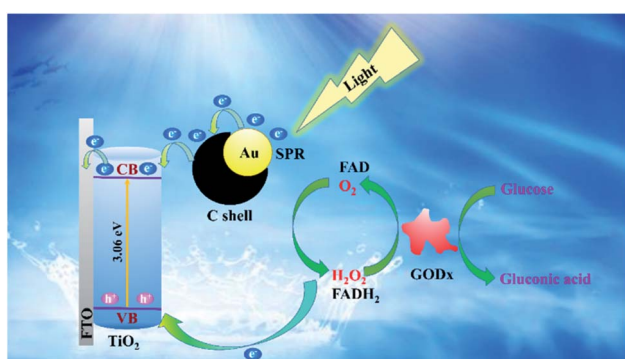
In summary, our research has successfully developed a PEC biosensor for Glu on the basis of a type of Au@C/TiO₂ composite, which had been synthesized using a common secondary hydrothermal approach. The SPR of Au nanoparticles and the introduction of the C shell accelerated the electron transport rate. The C–Au-deposition on the surface of the TiO₂ decreased the recombination rate of hole–electron pairs. Their synergistic influence enhanced the performance of PEC, prolonged the lifetime of photogenerated electrons, and increased the concentration of carriers. As a result, the obtained GODx/Au@C/TiO₂/FTO PEC biosensor presented outstanding stability and satisfactory reproducibility. The range of linear measurement and the sensitivity were 0.1–1.6 mM and 29.76 $\mu\text{A mM}^{-1} \text{cm}^{-2}$, respectively, and the limit of detection was low (0.049 mM). The GODx/Au@C/TiO₂/FTO biosensor exhibited excellent performance in detecting Glu, which suggested a possible application potential in the prepared composite of the PEC biosensors. The C–Au-deposition on the surface of TiO₂ also laid the foundation for the application of other PEC biosensors.

Conflicts of interest

There are no conflicts to declare.

Acknowledgements

The authors thank associate professor Chao Zhen (Institute of Metal Research, Chinese Academy of Sciences) for providing constructive and valuable suggestions on this work. The authors thank Chinese Academy of Medical Sciences for the support. This research was financially supported by the Finance Science and Technology Project of Hainan Province (No. ZDYF2019161, 2018106 and 2019RC221), National Natural Science Foundation of China (No. 51762012, 81860373 and 51862006), Key Laboratory Open Project Fund of Hainan University (2019007), and Key laboratory and trauma (Hainan Medical University), Ministry of Education (Grant. KLET-201910).



Scheme 2 Mechanism of the PEC detection of glucose at the GODx/Au@C/TiO₂/FTO biosensor.



Notes and references

1 W.-W. Zhao, J.-J. Xu and H.-Y. Chen, *Chem. Rev.*, 2014, **114**, 7421–7441.

2 W.-w. Zhan, Q. Kuang, J.-z. Zhou, X.-j. Kong, Z.-x. Xie and L.-s. Zheng, *J. Am. Chem. Soc.*, 2013, **135**, 1926–1933.

3 T. Hisatomi, J. Kubota and K. Domen, *Chem. Soc. Rev.*, 2014, **43**, 7520–7535.

4 Y. Yan, Q. Liu, X. Du, J. Qian, H. Mao and K. Wang, *Anal. Chim. Acta*, 2015, **853**, 258–264.

5 S. Komathi, N. Muthuchamy, K. P. Lee and A. I. Gopalan, *Biosens. Bioelectron.*, 2016, **84**, 64–71.

6 Y. Wang, W. Wang, S. Wang, W. Chu, T. Wei, H. Tao, C. Zhang and Y. Sun, *Sens. Actuators, B*, 2016, **232**, 448–453.

7 Y. Xin, Z. Li, W. Wu, B. Fu, H. Wu and Z. Zhang, *Biosens. Bioelectron.*, 2017, **87**, 396–403.

8 J.-H. Lee, I.-C. Leu, M.-C. Hsu, Y.-W. Chung and M.-H. Hon, *J. Phys. Chem. B*, 2005, **109**, 13056–13059.

9 X. Zhang, V. Thavasi, S. G. Mhaisalkar and S. Ramakrishna, *Nanoscale*, 2012, **4**, 1707–1716.

10 M. S. Arif Sher Shah, K. Zhang, A. R. Park, K. S. Kim, N.-G. Park, J. H. Park and P. J. Yoo, *Nanoscale*, 2013, **5**, 5093–5101.

11 J. Fang, L. Xu, Z. Zhang, Y. Yuan, S. Cao, Z. Wang, L. Yin, Y. Liao and C. Xue, *ACS Appl. Mater. Interfaces*, 2013, **5**, 8088–8092.

12 X. Liu, R. Yan, J. Zhu, X. Huo and X. Wang, *Electrochim. Acta*, 2015, **173**, 260–267.

13 G.-C. Fan, M. Zhao, H. Zhu, J.-J. Shi, J.-R. Zhang and J.-J. Zhu, *J. Phys. Chem. C*, 2016, **120**, 15657–15665.

14 S. Çakar and M. Özcar, *J. Photochem. Photobiol. A*, 2017, **346**, 512–522.

15 J. Wang, *Chem. Rev.*, 2008, **108**, 814–825.

16 P. Wu, Y. He, H.-F. Wang and X.-P. Yan, *Anal. Chem.*, 2010, **82**, 1427–1433.

17 R. Ahmad, M.-S. Ahn and Y.-B. Hahn, *Electrochim. Commun.*, 2017, **77**, 107–111.

18 D. Geng, X. Bo and L. Guo, *Sens. Actuators, B*, 2017, **244**, 131–141.

19 Y.-C. Zhu, N. Zhang, Y.-F. Ruan, W.-W. Zhao, J.-J. Xu and H.-Y. Chen, *Anal. Chem.*, 2016, **88**, 5626–5630.

20 S. I. Mogal, V. G. Gandhi, M. Mishra, S. Tripathi, T. Shripathi, P. A. Joshi and D. O. Shah, *Ind. Eng. Chem. Res.*, 2014, **53**, 5749–5758.

21 B. Liu and E. S. Aydin, *J. Am. Chem. Soc.*, 2009, **131**, 3985–3990.

22 F. Wang, J. Zheng, J. Qiu, S. Liu, G. Chen, Y. Tong, F. Zhu and G. Ouyang, *ACS Appl. Mater. Interfaces*, 2017, **9**, 1840–1846.

23 C. Ye, Y. Bando, G. Shen and D. Golberg, *J. Phys. Chem. B*, 2006, **110**, 15146–15151.

24 A. V. Raghu, K. K. Karuppanan and B. Pullithadathil, *Adv. Mater. Interfaces*, 2019, **6**, 1801714.

25 S. K. Parayil, H. S. Kibombo, C.-M. Wu, R. Peng, J. Baltrusaitis and R. T. Koodali, *Int. J. Hydrogen Energy*, 2012, **37**, 8257–8267.

26 M.-C. Daniel and D. Astruc, *Chem. Rev.*, 2004, **104**, 293–346.

27 B. H. Meekins and P. V. Kamat, *ACS Nano*, 2009, **3**, 3437–3446.

28 G. Wang, Q. Wang, W. Lu and J. Li, *J. Phys. Chem. B*, 2006, **110**, 22029–22034.

29 Z. Yang, Y. Ren, Y. Zhang, J. Li, H. Li, X. H. X. Hu and Q. Xu, *Biosens. Bioelectron.*, 2011, **26**, 4337–4341.

30 R. Zhao, X. Liu, J. Zhang, J. Zhu and D. K. Y. Wong, *Electrochim. Acta*, 2015, **163**, 64–70.

31 Y. Wang, L. Liu, M. Li, S. Xu and F. Gao, *Biosens. Bioelectron.*, 2011, **30**, 107–111.

32 Z. Yang, Y. Tang, J. Li, Y. Zhang and X. Hu, *Biosens. Bioelectron.*, 2014, **54**, 528–533.

33 S. Deng, G. Jian, J. Lei, Z. Hu and H. Ju, *Biosens. Bioelectron.*, 2009, **25**, 373–377.

